Fabio Altomare and Albert M. Chang

One-Dimensional Superconductivity in Nanowires

Related Titles

Bezryadin, A.

Superconductivity in Nanowires
Fabrication and Quantum Transport

2012
ISBN: 978-3-527-40832-0

Bhattachariya, R., Parantharam, M.P.

High Temperature Superconductors

2010
ISBN 978-3-527-40827-6

Luryi, S., Xu, J., Zaslavsky, A.

Future Trends in Microelectronics
Up the Nano Creek

2007
ISBN: 978-0-470-08146-4

Wolf, E. L.

Nanophysics and Nanotechnology
An Introduction to Modern Concepts in Nanoscience

2006
ISBN: 978-3-527-40651-7

Wong, B., Mittal, A., Cao, Y., Starr, G. W.

Nano-CMOS Circuit and Physical Design

2004
ISBN: 978-0-471-46610-9

Buckel, W., Kleiner, R.

Superconductivity
Fundamentals and Applications

2004
ISBN: 978-3-527-40349-3

Reich, S., Thomsen, C., Maultzsch, J.

Carbon Nanotubes
Basic Concepts and Physical Properties

2004
ISBN: 978-3-527-40386-8

Fabio Altomare and Albert M. Chang

One-Dimensional Superconductivity in Nanowires

WILEY-VCH Verlag GmbH & Co. KGaA

The Authors

Dr. Fabio Altomare
D-Wave Systems Inc.
100 - 4401 Still Creek Drive
Burnaby, BC, V5C 6G9
Canada

Prof. Albert M. Chang
Duke University
Department of Physics
Physics Building
Science Drive
Durham, NC 27708-0305
USA

Cover Figure
Artistic rendering of an 8 nm wide, 20 μm long nanowire fabricated on an InP semiconducting stencil. Electrical contacts to the nanowire (left and right pads) are realized during the nanowire deposition. At the center, a QPS junction is current biased by a current source: The number of windings of the phase of the order parameter decreases because of a phase slippage event. The diagram does not indicate the actual nanowire connection in a circuit. Rendering of the windings courtesy of A. Del Maestro.

Library of Congress Card No.:
applied for

British Library Cataloguing-in-Publication Data:
A catalogue record for this book is available from the British Library.

Bibliographic information published by the Deutsche Nationalbibliothek
The Deutsche Nationalbibliothek lists this publication in the Deutsche Nationalbibliografie; detailed bibliographic data are available on the Internet at http://dnb.d-nb.de.

Composition le-tex publishing services GmbH, Leipzig
Printing and Binding betz-druck GmbH, Darmstadt
Cover Design Adam-Design, Weinheim

Print ISBN 978-3-527-40995-2
ePDF ISBN 978-3-527-64907-5
ePub ISBN 978-3-527-64906-8
mobi ISBN 978-3-527-64905-1
oBook ISBN 978-3-527-64904-4

Printed in the Federal Republic of Germany
Printed on acid-free paper

To Maria Elena, Mattia, Gabriele, Giulia and to my parents:
Thank you for your love and support.

Fabio

To my family: Ying, Emily and Austin, my sister Margaret, my brother Winston, my father Bertrand Tsu-Shen, and my late mother, Virginia Pang-Ying.

Albert

Contents

Preface *XI*

Abbreviations and Symbols *XV*

Color Plates *XXI*

Part One Theoretical Aspects of Superconductivity in 1D Nanowires *1*

1 Superconductivity: Basics and Formulation *3*
1.1 Introduction *3*
1.2 BCS Theory *4*
1.3 Bogoliubov–de Gennes Equations – Quasiparticle Excitations *8*
1.4 Ginzburg–Landau Theory *10*
1.4.1 Time-Dependent Ginzburg–Landau Theory *12*
1.5 Gorkov Green's Functions, Eilenberger–Larkin–Ovchinnikov Equations, and the Usadel Equation *12*
1.6 Path Integral Formulation *19*
References *27*

2 1D Superconductivity: Basic Notions *31*
2.1 Introduction *31*
2.2 Shape Resonances – Oscillations in Superconductivity Properties *33*
2.2.1 Early Treatments of Shape Resonances in 2D Films *35*
2.2.2 Bogoliubov–de Gennes Equations, Finite Temperature, and Parabolic-Band Approximation for Realistic Materials *40*
2.2.3 Numerical Solutions and Thin Film Shape Resonances *42*
2.2.4 1D Nanowires – Shape Resonances and Size Oscillations *45*
2.3 Superconductivity in Carbon Nanotubes – Single-Walled Bundles and Individual Multiwalled Nanotubes *48*
2.4 Phase Slips *50*
2.4.1 Finite Voltage in a Superconducting Wire and Phase Slip *51*
2.4.2 Phase Slip in a Josephson Junction *52*
2.4.3 Langer–Ambegaokar Free Energy Minima in the Ginzburg–Landau Approximation *55*
2.4.4 Transition Rate and Free Energy Barrier *59*

2.4.5 Free Energy Barrier for a Phase Slip in the Ginzburg–Landau Theory *60*
2.4.6 Physical Scenario of a Thermally-Activated Phase Slip *64*
2.4.7 McCumber–Halperin Estimate of the Attempt Frequency *66*
References *71*

3 Quantum Phase Slips and Quantum Phase Transitions *75*
3.1 Introduction *75*
3.2 Zaikin–Golubev Theory *79*
3.2.1 Derivation of the Low Energy Effective Action *80*
3.2.2 Core Contribution to the QPS Action *88*
3.2.3 Hydrodynamic Contribution to the Phase-Slip Action *91*
3.2.4 Quantum Phase-Slip Rate *92*
3.2.5 Quantum Phase-Slip Interaction and Quantum-Phase Transitions *95*
3.2.6 Wire Resistance and Nonlinear Voltage–Current Relations *97*
3.3 Short-Wire Superconductor–Insulator Transition: Büchler, Geshkenbein and Blatter Theory *100*
3.4 Refael, Demler, Oreg, Fisher Theory – 1D Josephson Junction Chains and Nanowires *105*
3.4.1 Discrete Model of 1D Josephson Junction Chains *107*
3.4.2 Resistance of the Josephson Junctions and the Nanowire *114*
3.4.3 Mean Field Theory of the Short-Wire SIT *116*
3.5 Khlebnikov–Pryadko Theory – Momentum Conservation *121*
3.5.1 Gross–Pitaevskii Model and Quantum Phase Slips *123*
3.5.2 Disorder Averaging, Quantum Phase Transition and Scaling for the Resistance and Current–Voltage Relations *126*
3.5.3 Short Wires – Linear QPS Interaction and Exponential QPS Rate *130*
3.6 Quantum Criticality and Pair-Breaking – Universal Conductance and Thermal Transport in Short Wires *136*
References *143*

4 Duality *149*
4.1 Introduction *149*
4.2 Mooij–Nazarov Theory of Duality – QPS Junctions *152*
4.2.1 QPS Junction Voltage-Charge Relationship and Shapiro Current Steps *156*
4.2.2 QPS Qubits *157*
4.3 Khlebnikov Theory of Interacting Phase Slips in Short Wires: Quark Confinement Physics *159*
References *165*

5 Proximity Related Phenomena *167*
5.1 Introduction *167*
5.2 Transport Properties of Normal-Superconducting Nanowire-Normal (N-SCNW-N) Junctions *169*
5.2.1 Nonequilibrium Usadel Equations *169*
5.2.2 Parameterization of the Usadel Equations *174*

5.2.3 Numerical Results *175*
5.3 Superconductor–Semiconductor Nanowire–Superconductor Junctions *179*
5.4 Majorana Fermion in S-SmNW-S Systems with Strong Spin–Orbit Interaction in the Semiconductor *184*
References *188*

Part Two Review of Experiments on 1D Superconductivity *193*

6 Experimental Technique for Nanowire Fabrication *195*
6.1 Experimental Technique for the Fabrication of Ultra Narrow Nanowires *195*
6.2 Introduction to the Techniques *196*
6.2.1 Lithography *197*
6.2.2 Metal Deposition *198*
6.2.3 Etching *199*
6.2.4 Putting It All Together *199*
6.3 Step-Edge Lithographic Technique *201*
6.4 Molecular Templating *202*
6.5 Semiconducting Stencils *205*
6.6 Natelson and Willet *205*
6.7 SNAP Technique *206*
6.8 Chang and Altomare *208*
6.9 Template Synthesis *209*
6.10 Other Methods *211*
6.10.1 Ion Beam Polishing *211*
6.10.2 Angled Evaporation *213*
6.10.3 Resist Development *213*
6.11 Future Developments *214*
References *216*

7 Experimental Review of Experiments on 1D Superconducting Nanowires *219*
7.1 Introduction *219*
7.2 Filtering *220*
7.3 Phase Slips *221*
7.4 Overview of the Experimental Results *223*
7.4.1 Giordano's Experiments *225*
7.4.2 Recent Experiments on QPS *226*
7.4.3 QPS Probed via Switching Current Measurements *239*
7.5 Other Effects in 1D Superconducting Nanowires *248*
7.5.1 S-Shaped Current–Voltage Characteristic *248*
7.6 Antiproximity Effect *250*
7.6.1 Stabilization of Superconductivity by a Magnetic Field *253*
7.6.2 Shape Resonance Effects *255*
References *257*

8 Coherent Quantum Phase Slips *263*
8.1 Introduction *263*
8.2 A Single-Charge Transistor Based on the Charge-Phase Duality of a Superconducting Nanowire Circuit *263*
8.3 Quantum Phase-Slip Phenomenon in Ultranarrow Superconducting Nanorings *266*
8.4 Coherent Quantum Phase Slip *267*
8.5 Conclusion *272*
References *273*

9 1D Superconductivity in a Related System *275*
9.1 Introduction *275*
9.2 Carbon Nanotubes *275*
9.2.1 Proximity Effects in SWNT *276*
9.2.2 Intrinsic Superconductivity in SWNT *278*
9.2.3 Superconductivity in Ropes Mediated by the Environment *281*
9.3 Majorana Experiments *286*
9.3.1 Majorana Experiment in Semiconducting Nanowires *286*
9.3.2 Majorana Experiment in Hybrid Superconductor-Topological Insulator Devices *290*
9.4 Superconducting Nanowires as Single-Photon Detectors *292*
References *297*

10 Concluding Remarks *301*

Index *303*

Preface

This book is devoted to the topic of superconductivity in very narrow metallic wires. Interest in such wires is driven by the continuing drive for miniaturization in the electronics industry, where the reduction of heat dissipation by the use of interconnects which are superconducting may be necessary. This has led to the invention of new methods of producing very narrow wires with good quality and uniformity in dimensions, and opened up the possibility of novel device paradigms.

The superconducting state is a state of coherent pairs of electrons, held together by the mechanism of the Cooper instability. When the lateral dimensions are small, a new pathway opens up for the superconductor to produce dissipation, associated with the enhanced rate at which fluctuations can occur in the complex order parameter – a quantity which describes the magnitude and phase of the Cooper pairs. In many regimes, the fluctuations of the phase of the Cooper pairs is often the dominant process, in analogy with what occurs in dissipative Josephson junctions. This new pathway is related with the motion of vortices in type-II superconductors, which gives rise to dissipation in 2D (two-dimensional) and bulk superconductors, in which a rapid change of phase occurs as a vortex passes by. Here, because of the physical dimension of the system (comparable to 10 nm), the vortex quickly passes across the entire narrow wire, producing dissipation in the process.

Although nanowires are small in their transverse dimensions, they are still much larger than the Fermi wavelength (λ_F) of the electronic system, which is of the order of a few angstrom in all metals. In conventional superconductors such as Al, Pb, Sn, Nb, MoGe, and so on, in thin film or nanowire form, the coherence length is $\xi \approx 5-100$ nm, typically 10–1000 times the Fermi wavelength. The system we will consider is therefore in a sort of mixed-dimensional regime. From the condensate perspective, the system is 1D (one-dimensional), in the sense that the transverse dimensions are smaller than the Cooper pair size: for this reason, the wave function, or alternatively, the order parameter, describing the Cooper pairs, is uniform, and thus position-independent, in the transverse directions. From the fermionic quasiparticle excitation perspective, the system is effectively 3D (three-dimensional; λ_F is much smaller than the lateral dimension) and there is a large number of transverse channels (from $\approx$ 100 in a multiwalled carbon nanotube, to $\approx$ 3000 in an $\approx$ 8 nm diameter aluminum nanowire), analogous to transverse modes in a wave guide.

In this limit, the dominant collective excitations are no longer pair-breaking excitations across the superconducting energy gap, but rather "phase-slips," which are topological defects in the ground state configuration. Phase slips are related to the motion of vortices in type-II superconductors which give rise to dissipation in 2D and bulk superconductors: in a 1D system, they produce a sudden change of phase by 2π across a core region of reduced superconducting correlation which gives rise to a voltage pulse.

Another intriguing aspect arises from the fact that even in wires which are not ballistic along the wire length, the typical level spacing in the transverse direction can significantly exceed the superconducting gap energy scale. Thus, the possibility of singularity in the density of the electronic state in the normal system associated with each transverse channel can cause oscillatory behaviors in the superconducting properties.

From the above discussion, it is clear that the regime of interest is delineated by the condition that the size of the Cooper pairs, or the superconducting coherence length, be larger than the transverse directions perpendicular to the length of the wire. In this limit the order behavior of the Cooper pair is largely uniform across the wire length, and only variations along the wire length need to be considered. At temperatures well below the superconducting transition temperature, the scale for the observation of dimensionality effects is in the 10–100 nm range (5–50 nm in radius): in this regime, new physics have been predicted, including universal scaling laws in the conductance of the wire.

To access the regime where quantum processes become dominant, however, a more stringent requirement is necessary, that of a sufficiently large probability of fluctuations to occur: this more stringent criterion places the scale requirement in the 10 nm (5 nm in radius) range. Nanowires in this regime may either be a single monolithic wire, such as nanowires made of MoGe, Al, Nb, In, PbIn, Sn, and so on, or coupled wires such as in carbon nanotube bundles.

It should be noted that, in the strict sense, only systems in 2D or 3D have a true, sharp, thermodynamic phase transition into the superconducting state at a finite temperature T_c. In the 2D case, it is a Berenzinskii–Thouless–Kosterlitz type of second-order phase transition, while in 3D, it is a second-order continuous phase transition in the Ginzburg–Landau sense, at least for type-II superconductors supporting the existence of vortices within the bulk. In contrast, in a 1D nanowire, the fluctuations cause the transition to become smeared, so that the resistance remains finite, albeit small, below the transition. Early theoretical analyses were motivated by experimental observations of such behavior, and attempted to quantify the amount of residual resistance. Thus, naturally, questions arise as to whether the resistance vanishes at zero T, and whether novel excitations are able to limit the supercurrent below the depairing limit.

From a broader point of view, 1D superconducting nanowires are interesting from a variety of perspectives, including many body physics, quantum phase transition (QPT), macroscopic quantum tunneling (MQT) processes, and device applications. The field, by nature, involves rather technically sophisticated methods. This is true from either the experimental or theoretical side.

On the experimental side, there are many technical challenges, and thus it is not for the faint of heart. Such challenges include nanowire fabrication, the delicate nature of nanowires with respect to damage–they act as excellent fuses, and their sensitivity to environmental interference from external noise sources, and so on. At the level of 10 nm in transverse dimensions, corresponding roughly to 40 atoms across, even width fluctuations of a few atoms can have significant influence on the energetics and properties. Thus, to obtain intrinsic behaviors of relevance to a uniform wire, rather than behavior limited to weak-links or a very thin region in a nonuniform wire, fabrication is exceedingly demanding. Arguably, only in recent years has the emergence of fabrication techniques come into existence with sufficient precision for producing unusually uniform nanowires. Thus, substantial progress is occurring on the experimental front.

On the theoretical side, analyses invariably involve sophisticated quantum field theory (QFT), quantum phase transition (QPT), Bogoliubov–de Gennes BdG, Ginzburg–Landau (GL), Gorkov–Eilenberger–Usadel self-consistent (including nonlinearities) techniques, all of which require a rather advanced level of understanding of the theoretical machinery. This is often compounded by the fact that the concept of the quantum-mechanical tunneling in the phase of the superconducting order-parameter is difficult to motivate from a classical perspective, since, unlike coordinates or momenta, the phase is a concept born out of wave mechanics. Instead, the tunneling in the phase degree of freedom is usually introduced via the Feynman path integral type of formulation, as one finds a more natural description, for this phenomenon, in terms of instantons in field theory language.

The goal of this book is to produce a relatively self-contained introduction to the experimental and theoretical aspects of the 1D superconducting nanowire system. The aim is to convey what the important issues are, from experimental, phenomenological, and theoretical aspects. Emphasis is placed on the basic concepts relevant and unique to 1D, on identifying novel behaviors and concepts in this unique system, as well as on the prospects for potentially new device applications based on such new concepts and behaviors. The latest experimental techniques and results in the field are summarized. On the theoretical side, much of the field theoretic methods for analyzing the various quantum phase transitions, such as superconductor–metal transitions, superconductor–insulation transitions, and so on, brought about by disorder, are highly technical and the details are beyond the scope of this book. Nevertheless, an attempt is made to summarize the relevant issues and predictions, to pave the way for understanding the formalisms and issues addressed in available journal literature. It is the hope of the authors that this book will serve as a starting point for those interested in joining this exciting field, as well as serving as a useful reference for active researchers.

To this end, our philosophy is to present the field as an active, exciting, and ongoing discourse, rather than one that is fully established. Thus, many of the concepts and experiments are still fraught with a certain degree of healthy controversy. Thus, an attempt is made to convey a sense of openness to the discourse in the field.

The book is organized as follows: Chapter 1 contains a brief history of the field, and a succinct summary of the various theoretical methodologies for understand-

ing conventional superconductivity. These methods are widely used in analyzing 1D superconducting nanowire systems. Chapter 2 is devoted to the basic concepts of 1D superconductivity, including size quantization and its influence on superconducting properties, leading to the phenomenon of shape resonances, the phase-slip phenomenon, which originated from an attempt to explain the broadened temperature transition and the finite voltage along the wire below but near the transition, as well as the conditions and relevant energy scales in molecular systems such as carbon nanotubes. In Chapter 3, the quantum theory based on path integral formulation is summarized. The various types of quantum phase transitions and competing physical scenarios are described. Chapter 4 explores new concepts and potentially new devices based on the idea of a duality between Cooper pairs and the phase slip. Novel QPS junctions are described. These are believed to offer new venues for a current version of the Shapiro steps, as well as a platform for qubits. Nonlinear and nonequilibrium effects based on the Usadel equations are described in Chapter 5.

On the experimental side, the all-important description of the state-of-the-art fabrication methodologies is presented in Chapter 6. Experimental techniques, such as filtering to remove external environmental noise are summarized in Chapter 7. Finally, in Chapter 8, we discuss the current state of experimental progress, and the many open questions, as well as future prospects. To conclude, in Chapter 9, we describe recent experimental results in superconducting nanowire single-photon detector that are now approaching the 1D superconducting limit and devices that are related to 1D superconductivity via the proximity effect: in this class, we find nanotubes and semiconducting nanowires, which have recently indicated of the presence of Majorana fermions.

The authors are indebted to Sergei Khlebnikov (Purdue University), in particular for sharing his insight and for providing helpful comments on the entire theory section. The authors acknowledge the help of (in alphabetical order) G. Berdiyorov (University of Antwerp), E. Demler (Harvard University), A. Del Maestro (University of Vermont), D. Golubev (Karlsruhe Institute of Technology), F. Peeters (University of Antwerp), G. Refael (Caltech), S. Sachdev (Harvard University), A. Zaikin (Lebedev Inst. of Physics and Karlsruhe Institute of Technology) for critically reading the manuscript. The authors would also like to thank M.R. Melloch (Purdue University), C.W. Tu (University of California at San Diego), P. Li, P.M. Wu, G. Finkelstein, Y. Bomze, I. Borzenets (Duke University), and Li Lu (Institute of Physics, CAS, Beijing) for their help and fruitful discussions.

September, 2012 *F. Altomare and A.M. Chang*

Abbreviations and Symbols

Acronyms

APE	Anti-proximity Effect
BdG	Bogoliubov–de–Gennes
BCS	Bardeen–Cooper–Schreiffer
CPR	Current–Phase Relation
cQPS	Coherent Quantum Phase-Slip
DCR	Dark Current Rate
DQM	Dissipative Quantum Mechanics
e-beam	Electron beam
GIO	Giordano expression for the resistance due to quantum phase slips, or to QPS and TAPS
GL	Ginzburg–Landau
HQS	Silsesquioxane, a type of negative electron beam resist
IRFP	Infinite-Randomness Fixed Point
JJ	Josephson Junction
KQPS	Khlebnikov Quantum Phase-Slip
KTB	Kosterlitz–Thouless–Berezinskii
LA	Langer–Ambegaokar
LAMH	Langer–Ambegaokar–McCumber–Halperin
MBE	Molecular-Beam-Epitaxy
MH	McCumber–Halperin
PMMA	Polymethylmethacrylate: probably the most common electron beam resist, mainly used as positive tone resist
PSC	Phase-Slip Center
QPS	Quantum Phase-Slip
RTFIM	Random-Transverse-Field Ising Model
SC	Superconducting
SG	sine-Gordon
SEM	Scanning Electron Microscope
SIT	Superconductor-Insulator Transition

SmNW	Semiconducting Nanowire
SMT	Superconductor-Metal Transition
SNAP	Superlattice Nanowire Pattern Transfer
SNAP	Superconducting Nanowire Avalanche Photo Detector
SNSPD	Superconducting Nanowire Single-Photon Detector
SQUID	Superconducting Interference Device
SSPD	Superconducting Single-Photon Detector
SWNT	Single-Walled Nanotube
SWCNT	Single-Walled Carbon Nanotube
TAP or TAPS	Thermally-Activated Phase Slip

Symbols

w	Width of nanowire or wire
h	Height of nanowire or thin film
d	Diameter of nanowire
L	Length of nanowire
L_x	Length in x-direction of a thin film
L_y	Length in y-direction of a thin film
A	Cross sectional area of a nanowire
V	Volume
T	Temperature
$k_B T$	Thermal energy scale; k_B is the Boltzmann's constant
β	$\frac{1}{k_B T}$
e	fundamental unit of charge: $+1.602 \times 10^{-19}$ C = $+ 4.80 \times 10^{-10}$ esu
μ	(i) Chemical potential (ii) parameter that controls the KTB (Kosterlitz–Thouless–Berezinskii) phase transition
E_F	Fermi energy
v_F	Fermi velocity (speed)
$N(0) \equiv D(E_F)$	Density of states at the Fermi level of both spins, in the normal state
$-e$	Charge of the electron
$(-2e)$	Charge of the Cooper-pair of electrons
m	electron mass
M	Cooper-pair mass $M = 2m$
$D = \frac{1}{3} v_F l_{mfp}$	Diffusion coefficient
l_{mfp}	Mean-free-path
T_c	Critical temperature, or normal to superconducting transition temperature
Δ	Superconducting gap
Δ_0	Zero temperature superconducting gap

ω_D	Debye frequency
n_s	Superconducting carrier density
g	Gorkov coupling constant, take to be positive $g = \mathcal{V}V$
u	Amplitude of electron-like component of a Bogoliubov quasiparticle
v	Amplitude of hole-like component of a Bogoliubov quasiparticle
ξ	Superconducting coherence length, usually in the dirty limit of $\xi_{cln} \sim \xi_{bulk} \sim \xi_{BCS} \gg l_{mfp}$
ξ_0	Zero temperature superconducting coherence length
ξ_{bulk}	Superconducting coherence length is bulk 3D material
ξ_{cln}	Superconducting coherence length in the clean limit
ξ_{BCS}	The BCS superconducting coherence length
λ_L	London penetration depth
λ_n or λ_i	Eigenvalues of index n or index i
E_C	Coulomb charging energy $E_C = (2e)^2/C$, where C is the capacitance
E_J	Josephson energy
C	(i) Capacitance per unit length of a nanowire (ii) capacitance of a Josephson junction
L_{kin}	Kinetic inductance per unit length of a nanowire
c_{pl}	Mooij–Schön plasmon mode propagation speed
ψ or $\psi^\dagger$	Electron annihilation or creation operator
ψ	(i) Ginzburg–Landau superconducting order parameter (dimensionless) (ii) Gross–Pitaevskii superconducting order parameter
$\boldsymbol{\Psi}$	Ginzburg–Landau superconducting order parameter
τ_{GL}	Ginzburg–Landau relaxation time: $\tau_{GL} = \frac{\pi}{8}\frac{\hbar}{T_c - T}$
ϕ_0	Superconducting flux quantum: $\phi_0 = hc/(2e)$ (cgs); $\phi_0 = h/(2e)$ (SI)
R_Q	Superconducting quantum resistance $R_Q \equiv h/(2e)^2 \approx 6.453\,\mathrm{k\Omega}$
A	Vector potential
V	(i) electrostatic potential (ii) strength of electron-phonon coupling in the Gorkov coupling constant $g = \mathcal{V}V$
$\boldsymbol{E}$	Electric field
$\boldsymbol{B}$	Magnetic field
J	Electrical current density
J_s	Electrical current density of the superfluid
J_c	Critical electrical current density
j	Reduced electrical current density
j_c	Reduced critical electrical current density
I	Electrical current
I_c	Critical electrical current

I_s	Switching current, at which a nanowire switches from a superconducting state to a normal state, typically somewhat smaller than the I_c in the depairing limit
I_{bias}	Externally applied bias current
a	(i) Lattice constant (ii) Proportionality constant in the Giordano expression for the quantum phase-slip rate or quantum phase-slip resistance
φ	Phase of the complex superconducting order-parameter
H_c	Thermodynamic critical (magnetic) field
R_{QPS}	The quantum phase-slip contribution to the resistance
R_{TAP}	The thermally-activated phase-slip contribution to the resistance
Γ_{QPS}	The quantum phase-slip (tunneling) rate
Γ_{TAP}	The phase-slip rate due to thermal-activation
$\Gamma^{\pm}$	The phase-slip rate: + corresponds to increasing the phase-winding by one unit, − to decreasing by one unit
Γ_{inst}	Quantum tunneling rate of an instanton
Ω	Attempt frequency for the phase-slip process
$\Omega^{\pm}$	Attempt frequency for the phase-slip process: + corresponds to increasing the phase-winding by one unit, − to decreasing by one unit
Z	(i) Partition function (ii) Mooij–Schön plasmon propagation impedance
S	Action, in almost all cases, the Euclidean action in the imaginary-time formulation
S_D	Drude contribution to the action
S_J	Josephson contribution to the action
S_L	London contribution to the action
S_{em}	Electromagnetic field contribution to the action
S_{diss}	Dissipation contribution to the action
S_{bias}	Contribution to the action from a biasing current
S_{bdry}	Boundary contribution to the action
S_{1D}	Action for a 1D superconducting nanowire
S_{QPS}	Action due to a single or multiple quantum phase-slip
F	Free energy
ΔF	Free energy barrier for the creation of a phase-slip
$\Delta F^{\pm}$	Free energy barrier for the creation of a phase-slip: + corresponds to increasing the phase-winding by one unit, − to decreasing by one unit
$\hat{G}$	The Gorkov Green's functions in matrix form in Nambu space
$\check{G}$	The Gorkov Green's functions in the Keldysh formulation, with both the advanced and retarded, as well as the Keldysh component. The matrix is in the direct product space of forward and backward branches of the Keldysh contour, with the Nambu space.

G	The normal components of the Gorkov Green's functions. They represent the diagonal components of the $\hat{G}$ matrix
F	The superconducting components of the Gorkov Green's functions, representing the off-diagonal components of the $\hat{G}$ matrix (sometimes with an extra sign change, and or hermitian conjugation)
$G^{\mathrm{R,A,K}}$	In the Keldysh formulation: Retarded (R) G, Advanced (A) G, and Keldysh (K) G
$F^{\mathrm{R,A,K}}$	In the Keldysh formulation: Retarded (R) F, Advanced (A) F, and Keldysh (K) F
$\hat{g}$	The Eilenberger–Larkin–Ovchinnikov Green's functions, which are the Gorkov ones averaged over an energy variable
$\check{g}$	The Eilenberger–Larkin–Ovchinnikov Green's functions, which are the Gorkov ones averaged over an energy variable, in the Keldysh formulation, with both the advanced and retarded, as well as the Keldysh component. The matrix is in the direct product space of forward and backward branches of the Keldysh contour, with the Nambu space.
g	The normal components of the Eilenberger–Larkin–Ovchinnikov Green's functions, which are the Gorkov ones averaged over an energy variable. They represent the diagonal components of the $\hat{g}$ matrix
f	The superconducting components of the Eilenberger–Larkin–Ovchinnikov Green's functions, which are the Gorkov ones averaged over an energy variable, representing the off-diagonal components of the $\hat{g}$ matrix
σ	Electron spin index
$\sigma_{x,y,z}$	x: x-component of Pauli matrix; y: y-component, z: z-component
$g^{\mathrm{R,A,K}}$	In the Keldysh formulation: Retarded (R) g, Advanced (A) g, and Keldysh (K) g
$f^{\mathrm{R,A,K}}$	In the Keldysh formulation: Retarded (R) f, Advanced (A) f, and Keldysh (K) f
f_{QPS}	QPS fugacity
x_{o}	Core size of a quantum phase-slip, typically taken to be of order ξ_0
τ_0	Time-scale of a quantum phase-slip, typically $\gtrsim \hbar/\Delta$
D_{N}	Inverse of the compressibility of normal electron fluid
D_{S}	Inverse of the compressibility of superconducting electron fluid
V_{N}	Voltage of the normal fluid
V_{S}	Voltage of the super fluid
r	Normal electron to Cooper-pair conversion resistance
γ	Parameter proportional to the rate of normal electron to Cooper-pair conversion
λ_{Q}	Length scale for the normal electron to Cooper–pair conversion process

$f_{\mathrm{dpl,p}}$	Fugacity of QPS–anti-QPS dipoles, separated by p lattice sites
K or K_{s}	The superconducting stiffness
$K_{\mathrm{s,w}}$ or K_{w}	The superconducting stiffness for a 2D strip of width w
α_{dis}	Dimensionless disorder parameter in the Khlebnikov–Pryadko theory of quantum phase-slips
A_{dis}	A parameter, which characterizes the correlation integral of the disorder potential
C_{w}	Capacitance per unit area of a narrow 2D superconducting strip
$L_{\mathrm{kin,w}}$	Kinetic inductance for a unit area of a narrow 2D superconducting strip
q	Vortex charge-vector
$q^{0;1,1}$	The 0-th, 1st and 2nd components of the (2+1)D q-vector
J_{vor}	Vortex current density-vector
$f_{\mu\nu}$	The field tensor components of an effective photon field
n_{cp}	Cooper-pair number
n_{flux}	The flux number penetration a superconducting loop
ω_{pl}	Plasma frequency, e.g. in a Josephson junction, or that characterizing the vibrations within the local minimum of the free-energy
V_{c}	The critical voltage in a QPS-junction. It is the dual to the critical current I_{c} in a conventional Josephson Junction

Color Plates

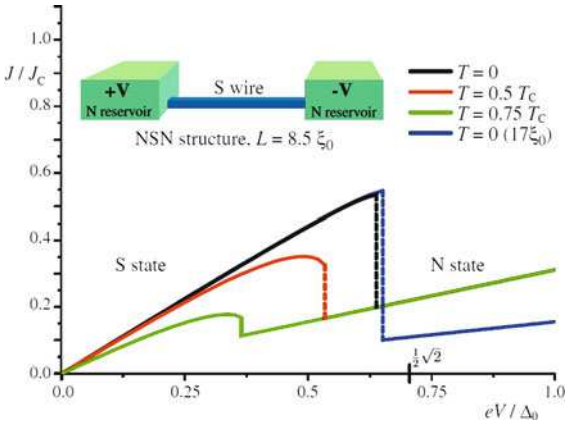

Figure 5.4 The calculated current (J)–voltage (V) relation of a superconducting wire of length $L = 8.5\xi_0$ between normal metallic reservoirs (see inset) at several temperatures, and for a wire of length $17\xi_0$. J_c is the critical current density, and Δ_0 the bulk gap energy. From [8].

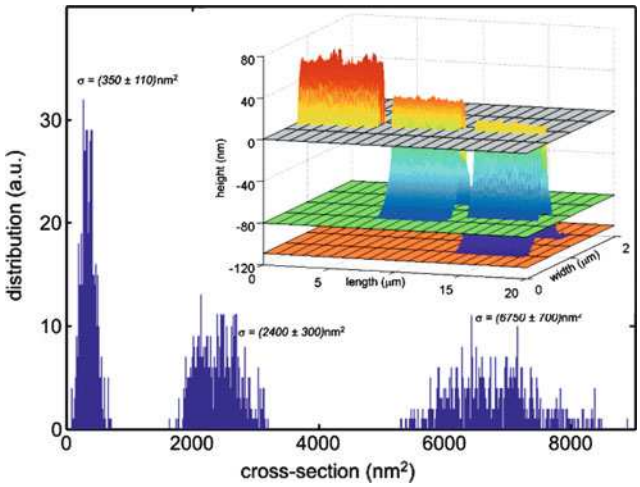

Figure 6.7 Histograms showing the distribution of the wire cross section before and after sputtering. To collect statistics, about 500 SPM (scanning probe microscope) scans were taken across the wire with the step along its axis $\sim$ 12 nm, which is comparable to the radius of curvature of the SPM tip. Narrowing of the histograms is due to the "polishing" effect of ion sputtering. The inset shows the evolution of the sample shape while sputtering measured by SPM. The bright color above the gray plane corresponds to Al and the blue below the plane to Si. Planes (gray, green, orange) indicate Si substrate base levels after successive sessions of sputtering. As Si is sputtered faster than Al, the wire is finally situated at the top of the Si pedestal. Gray plane (height = 0) separates Si from Al. From [39].

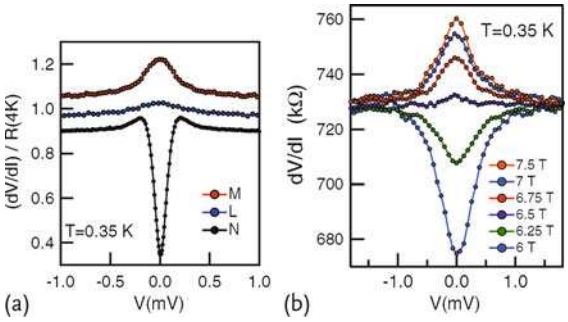

Figure 7.6 (a) Normalized differential resistance at $T = 0.35$ K for indicated MoGe wires (M, L insulating, N superconducting). Data for wires L and N are downshifted by 0.05 and 0.1, respectively. (b) Differential resistance as a function of bias voltage at $T = 0.35$ K in the transitional regime of the SIT for superconducting nanowires F. Adapted from [41].

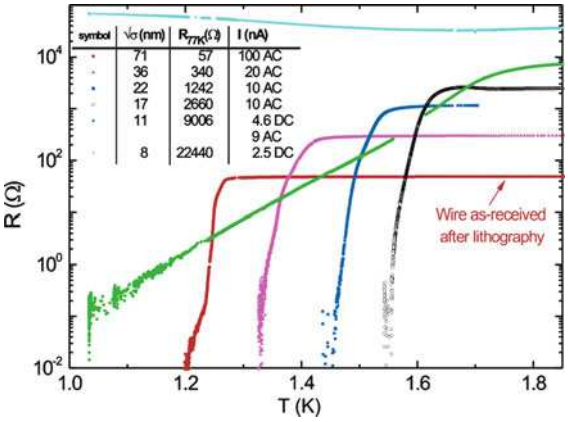

Figure 7.7 Resistance vs. temperature for the same aluminum wire of length $L = 10\,\mu m$ after several sputtering sessions. The sample and the measurement parameters are listed in the table. For low-Ohmic samples, lock-in AC measurements with the front-end preamplifier with input impedance 100 kΩ were used; for resistance above ∼ 500 Ω, a DC nanovolt preamplifier with input impedance ∼ 1 GΩ was used. The absence of data for the 11 nm sample at $T \sim 1.6$ K is due to switching from a DC to AC setup. Note the qualitative difference of $R(T)$ dependencies for the two thinnest wires from the thicker ones. From [34].

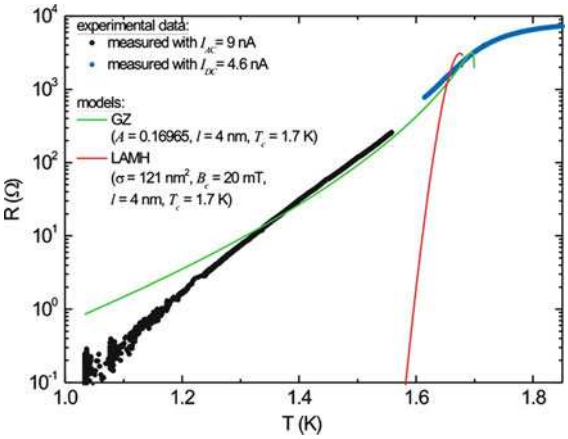

Figure 7.8 $R(T)$ dependence for the $\sqrt{\sigma} \sim 11$ nm aluminum sample. The green line shows the result of fitting to a renormalization theory (Reference 18 in [34]) with A, l, and T_c being the fitting parameters. The same set of parameters together with the critical magnetic field B_c measured experimentally is used to show the corresponding effect of thermally activated phase slips on the wire's $R(T)$ transition (red line) (References 1,2 in [34]). The parameter σ is obtained from the normal state resistance value and the known sample geometry (Reference 12 in [34]). The estimation for σ is in reasonable agreement with SPM analysis as well as with evolution of σ over all sputtering sessions (see Figure 7.7). From [34].

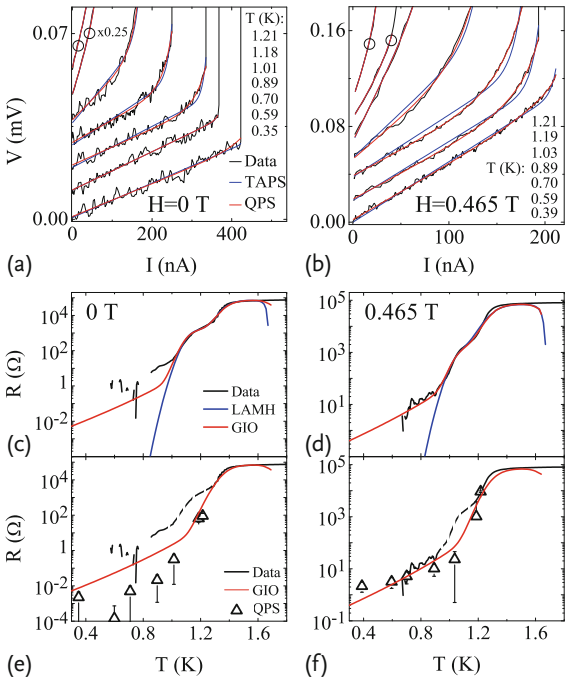

Figure 7.9 Nonlinear *I–V* curves and linear resistance for Al nanowire sample at different magnetic fields (H): Black curves – data; red curves – fits to the GIO (≡ GIO + LAMH; GIO denotes Giordano) expressions for QPS (≡ TAPS + QTPS; TAPS denotes thermal-activated phase-slips and QTPS quantum-tunneling of phase-slips), and blue curves – fits to the LAMH expressions for TAPS alone. (a) and (b) show *I–V* curves offset for clarity. The fits to QPS are of higher quality compared to TAPS; each fit includes a series resistance term V_S. These *I–V* curves can be fitted equally well by a power law form $V = V_S + (I/I_k)^{\nu}$ where $12 < \nu < 3.2$ for $0 \leq H \leq 1.05$ T [21, 37]. (c) and (d) show linear resistance after background subtraction (see Figure 1a in [24] and [37]). The LAMH fits are poor at low *T*. (e) and (f) show the resistance contribution due to phase slips (R_{QPS}) extracted in (a) and (b) from fits to the *I–V* curves using the GIO expressions (discrete points, Δ). RQPS and the linear resistance from (c) and (d) are refitted using the GIO expressions (red) with the same $a_{GIO}(= 1.2)$ while disregarding the irrelevant shoulder feature (dashed line). Adapted from [24].

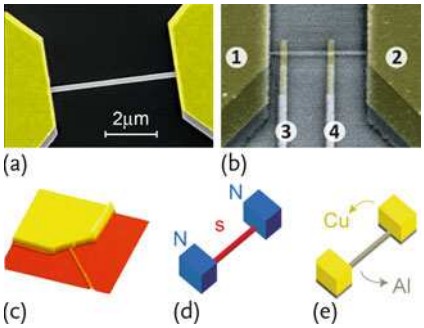

Figure 7.11 A superconducting Al nanowire connected to two massive normal reservoirs, consisting of the same Al, covered by a normal metal Cu layer: (a) SEM-picture, (c) AFM-picture, and (d) and (e) show a schematic representation. The thin Al of the pads is driven normal by the inverse proximity effect of the thick normal Cu. Normal tunneling probes are attached for local measurements (b). From [53].

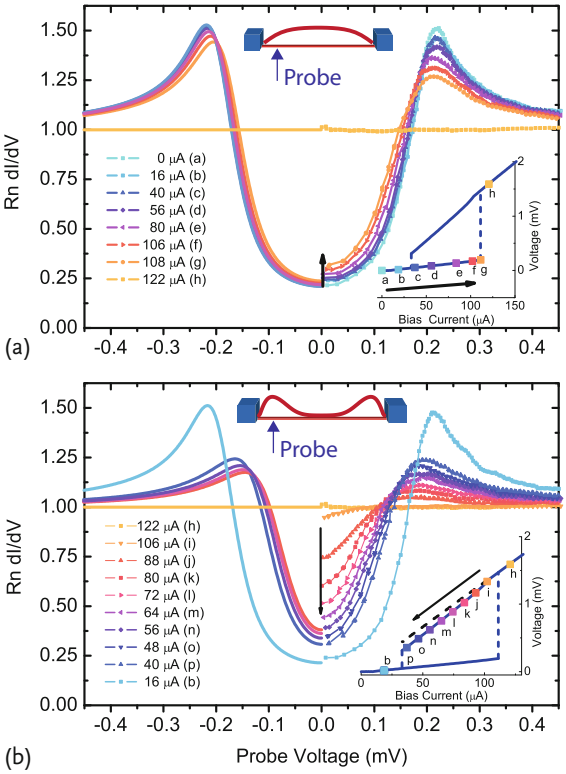

Figure 7.12 The local density of states (DOS $\propto dI/dV$) (a) the global superconducting state and (b) the bimodal state for different bias currents I_{12} of a 100 nm wider Al nanowire, measured at 200 mK. For the global superconducting state, the gap is only weakly dependent on the bias current, while for the bimodal state, for which only regions adjacent to the normal contacts are superconducting while the middle of the nanowire is in the normal state, one observes a DOS gradually changing from a normal into a superconducting state. From [53].

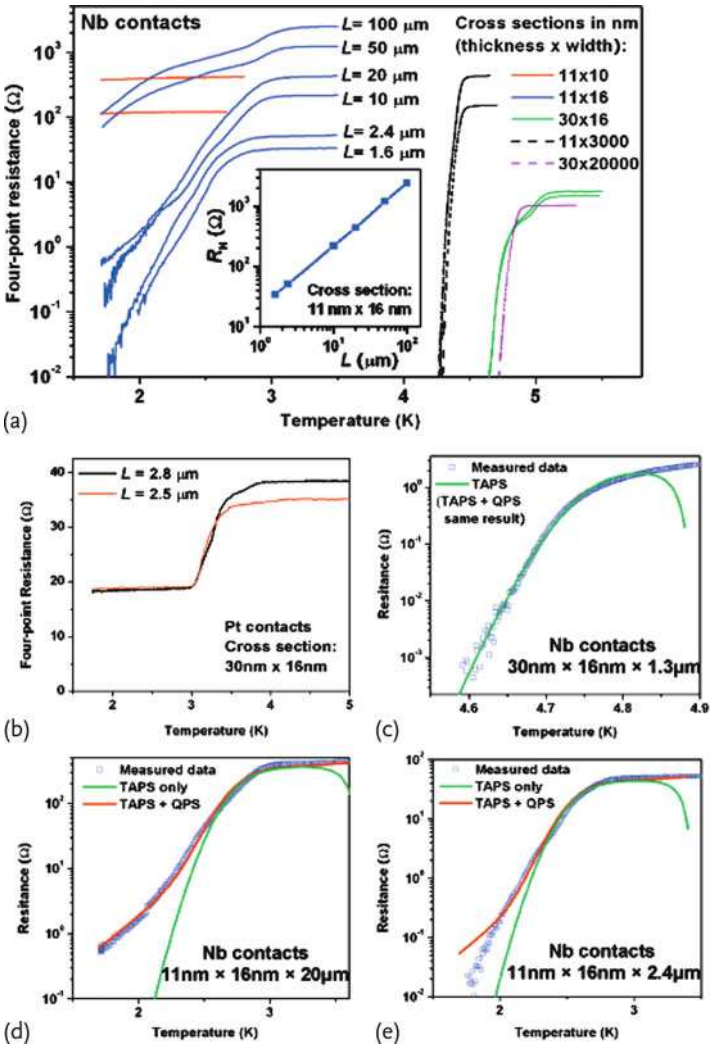

Figure 7.13 Temperature dependence for the four-point resistance of Nb NW arrays and films. (a) Superconducting Nb contacted NW arrays and films. Red lines: arrays of 12 NWs of cross section 11 nm × 10 nm and length L (from top to bottom) = 3 and 0.9 μm. Blue lines: arrays of 100 NWs of cross section 11 nm × 16 nm and L = 100, 50, 20, 10, 2.4, and 1.6 μm. Green lines: arrays of 250 NWs of cross section 30 nm × 16 nm and L = 1.5 and 1.3 μm. Black dashed lines: 11 nm thick films with width of 3 μm, L = 60 and 20 μm. Purple dashed line: a 30 nm thick film with a width of 20 μm, L = 2.5 μm. Inset: Length dependence of the normal-state resistance for arrays of 100 NWs of cross section 11 nm × 16 nm. (b) Normal-state Pt contacted NW arrays of cross section 30 nm × 16 nm. (c) 30 nm × 16 nm × 1.3 μm data in (a) fitted to TAPS theory (TAPS + QPS gives an indistinguishable result). (d) 11 nm × 16 nm × 20 μm data fitted to the theories. (e) 11 nm × 16 nm × 2.4 μm data fitted to the theories. From [40].

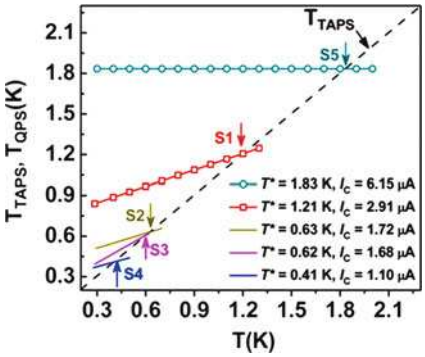

Figure 7.17 The best-fit effective temperature for fluctuations at different bath temperatures for five different $Mo_{1-x}Ge_x$ nanowire samples (S1–S5). For all TAPS rate calculations, the effective temperature is chosen as the bath temperature (shown by the black dashed line). For the QPS rates, the effective temperature TQPS, used in the corresponding QPS fits, similar to the blue-line fits of b [4], is shown by the solid lines. For each sample, below the crossover temperature T^* (indicated by arrows), QPS dominates the TAPS. They find that the T^* decreases with decreasing critical depairing current of the nanowires, which is the strongest proof of QPS. The trend indicates that the observed behavior of TQPS below T^* is not due to extraneous noise in the setup or granularity of wires, but, indeed, is due to QPS. Adapted from [4].

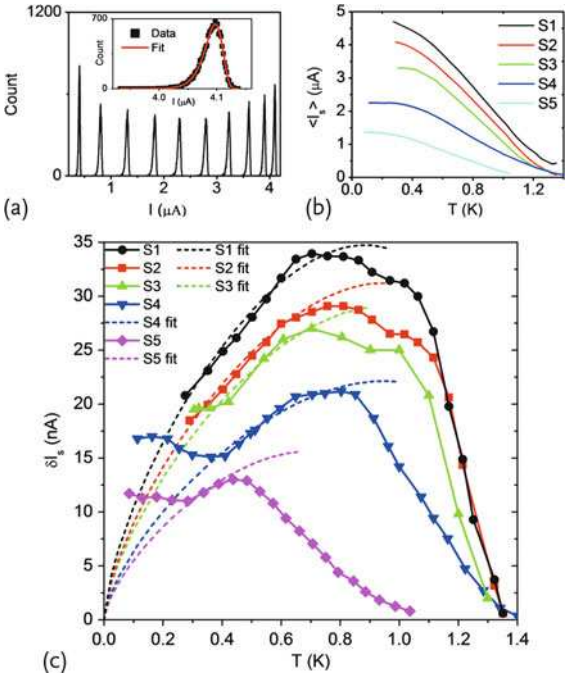

Figure 7.18 (a) I_s distribution for Al nanowire S2 at different temperatures: right to left: 0.3–1.2 K in 0.1 K increments. The inset shows the 0.3 K distribution, fitted by the Gumbel distribution (Reference 20 in [28]). (b) $\langle I_s \rangle$ vs. temperature – top to bottom S1–S5. (c) Symbols: δI_s vs. temperature. Dashed lines: fittings in the single TAPS regime using (Eq. 2 in [28]). An additional scale factor of 1.25, 1.11, 1.14, 0.98, and 1.0, for S1–S5, respectively (average 1.1 ± 0.1), is multiplied to match the data. Alternatively, a $\approx$ 6% adjustment in the exponent fits the data without the scale factor. Adapted from [28].

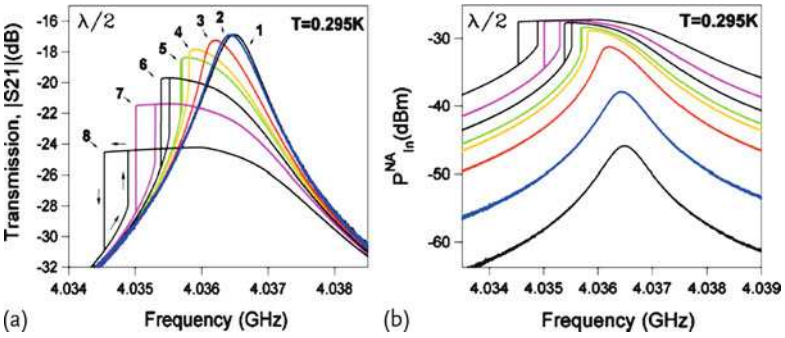

Figure 7.19 (a) ($Mo_{1-x}Ge_x$ sample S2) Transmission amplitude S_{21} (dB) in forward and backward frequency sweep for various driving powers. The graph shows Duffing bifurcation occurring at higher driving powers. The curves correspond to different driving powers: 1: $P^{NA}_{out} = -29$ dBm (black); 2: −21 dBm (blue); 3: −14 dBm (red); 4: −11 dBm (orange); 5: −10 dBm (green); 6: −8 dBm (black); 7: −6 dBm (violet); and 8: −3 dBm (black). (b) (sample S2) Replotting of the data from (a) as the transmitted power P^{NA}_{in} measured at the network analyzer input vs. frequency. From [60].

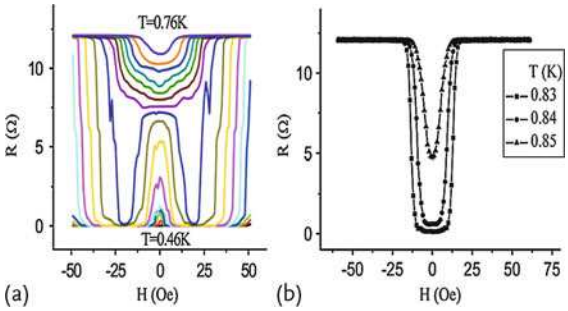

Figure 7.25 (a) Magnetic-field dependence of Zn wire resistance, at a high current $I \approx 4.4$ μA, with temperatures ranging from 0.46 to 0.76 K, every 0.02 K. (b) Magnetic-field dependence of wire resistance, at a low current $I = 0.4$ μA, with temperatures ranging from 0.83 to 0.85 K, every 0.01 K. From [31].

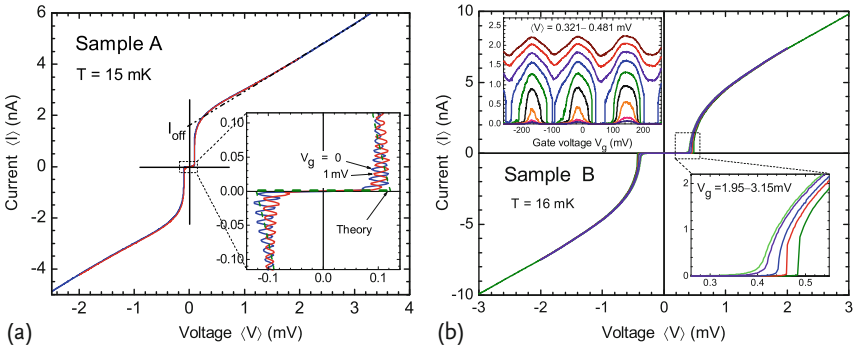

Figure 8.3 (a) The charge-modulated *I–V* curves of sample A recorded in a current-bias regime for two gate voltages shifted by a half-period. In the region of small currents (enlarged in the inset), one can see the modulation with period $\Delta I = 13.5$ pA, which is due to the asymmetry of off-chip biasing circuitry, resulting in the current dependence of the electric potential of the transistor island, $\delta V = (R_{bias1} - R_{bias2})I$ and, therefore, of the effective gate charge, $\delta Q_g = (C_g + C_0)\delta V$. The green dashed line shows the shape of the bare *I–V* curve given by the RSJ model (Equation 10 in [5]) with fixed Q_g. (b) The *I–V* curves of sample B measured in the voltage bias regime at different values of gate voltage V_g. The bottom right inset shows details of the Coulomb blockade corner. Upper left inset: the gate voltage dependence of the transistor current measured at different bias voltages V_b, providing a steady increase of $\langle V \rangle$ from 0.321 up to 0.481 mV in 20 μV steps (from bottom to top). Adapted from [5].

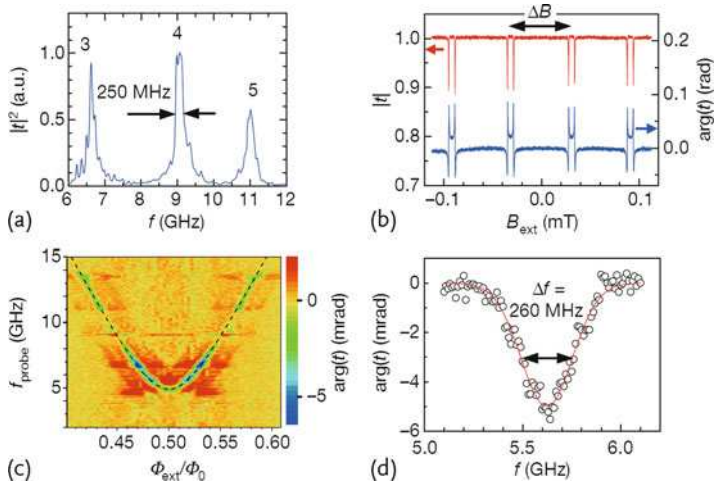

Figure 8.8 Experimental data. (a) Power transmission through the resonator measured within the bandwidth of our experimental setup. Peaks in transmission power coefficient, $|t|^2$, correspond to resonator modes, with mode number m indicated for each peak (a.u., namely, arbitrary units). (b) Transmission through the resonator as function a of external magnetic field B_{ext} at $m = 4$ ($f_4 = 9.08\,\text{GHz}$). The periodic structure in amplitude ($|t|$) and phase ($\arg(t)$) corresponds to the points where the lowest-level energy gap $\Delta E/h$ matches f_4. The period $\Delta B = 0.061\,\text{mT}$ ($= \Phi_0/S$) indicates that the response comes from the loop (shown in Figure 1b) with the effective loop area $S = 32\,\mu\text{m}^2$. (c) The two-level spectroscopy line obtained in two-tone measurements. The phase of transmission, $\arg(t)$, through the resonator at f_4 is monitored, while another tone with frequency f_{probe} from an additional microwave generator, and B_{ext}, are independently swept. The plot is filtered to eliminate the contribution of other resonances ($2 < m < 6$), visible as horizontal red features. The dashed line is the fit to the energy splitting, with $\Delta E/h = 4.9\,\text{GHz}$, $I_p = 24\,\text{nA}$. (d) The resonant dip is measured at $\Phi/\Phi_0 = 0.52$. The red curve is the Gaussian fit. From [14].

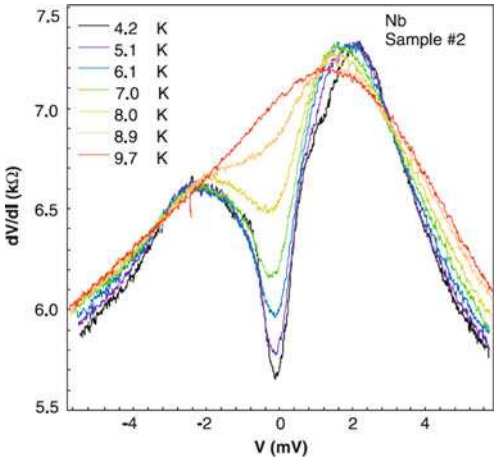

Figure 9.3 Differential resistance dV/dI vs. bias voltage V for a SWNT sample #2 of diameter $D < 1.8$ nm with Nb electrodes over a range of temperatures around T_c of Nb (9.2 K). The magnitude of the Andreev dip decreases with increasing T and disappears above T_c. From [5].

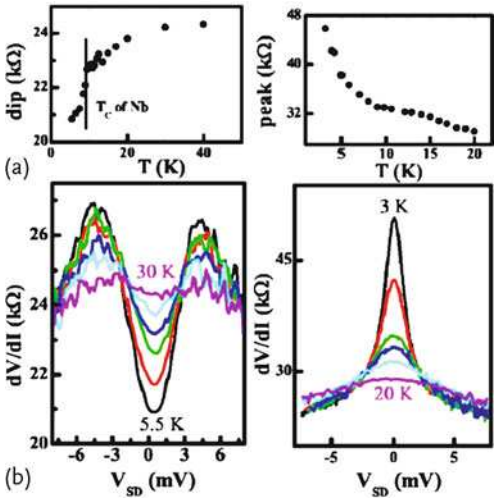

Figure 9.5 Differential resistance as a function of bias and temperature for CNFET (carbon nanotube field-effect-transistor) no. 1. $V_g = 47$ V for the dip on the left. $V_g = 48$ V for the peak on the right. The temperatures for the curves shown in (c) are 5.5, 8.5, 9.5, 15, 20, and 30 K. The temperatures for the curves shown in (d) 3, 4, 7, 9, 15, and 20 K. From [10].

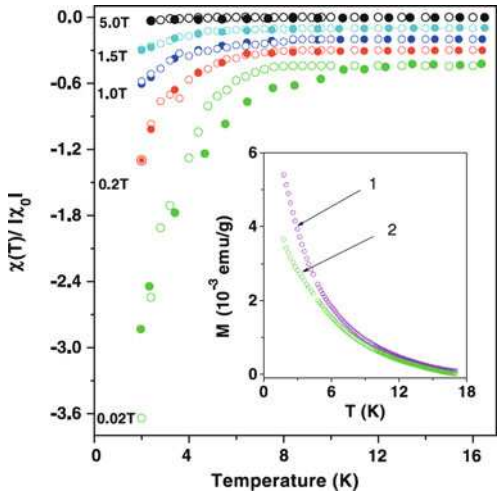

Figure 9.7 Normalized magnetic susceptibility of the SWNTs plotted as a function of temperature for five values of the magnetic field. The curves are displaced vertically for clarity. Values shown are for theory (open symbols) and experiment (filled symbols). χ_0 denotes the value of the susceptibility at $T = 1.6$ K and magnetic field $= 0.2$ T. The experimental value of χ_0, when normalized to the volume of the SWNTs, is -0.015 (in units where $B = 0$ denotes $\chi_0 = -1$). The scatter in the theory points reflects statistical fluctuations inherent in the Monte Carlo calculations. (Inset) Temperature dependence of magnetization density for zeolite AFI crystallites (curve 1) and for AFI crystallites with SWNTs in their channels (curve 2). Both curves are measured at 2000 Oe. From [13].

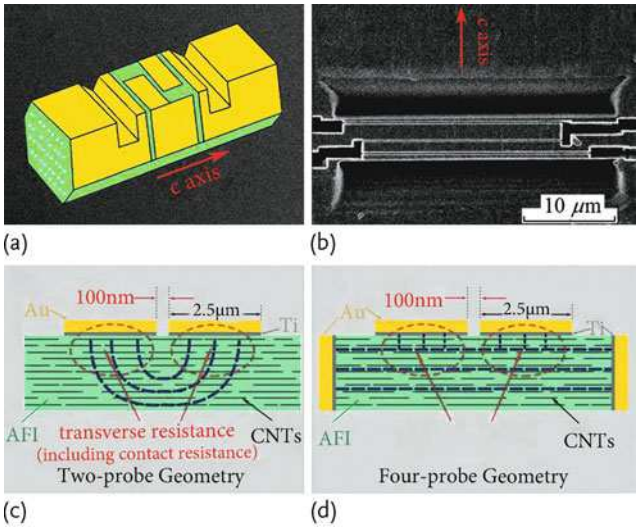

Figure 9.8 (a) Cartoon of the sample contain an array of SWNT in an AFI zeolite crystal. Yellow denotes gold and green denotes the AFI crystal surface exposed by FIB etching. Nanotubes are delineated schematically by open circles. (b) SEM image of one sample. The *c*-axis is along the N-S direction. The thin, light, horizontal line in the middle is the 100 nm separation between the two surface voltage electrodes that are on its two sides. The dark regions are the grooves cut by the FIB and sputtered with Au/Ti to serve as the end-contact current electrodes. (c) and (d) show schematic drawings of the two-probe and four-probe geometries, respectively. Blue-dashed lines represent the current paths. In (d), the two end-contact current pads are 4 mm in depth and 30 mm in width. The difference between the two-probe and the four-probe measurements is the transverse resistance, delineated by the red circles in (c). From [17].

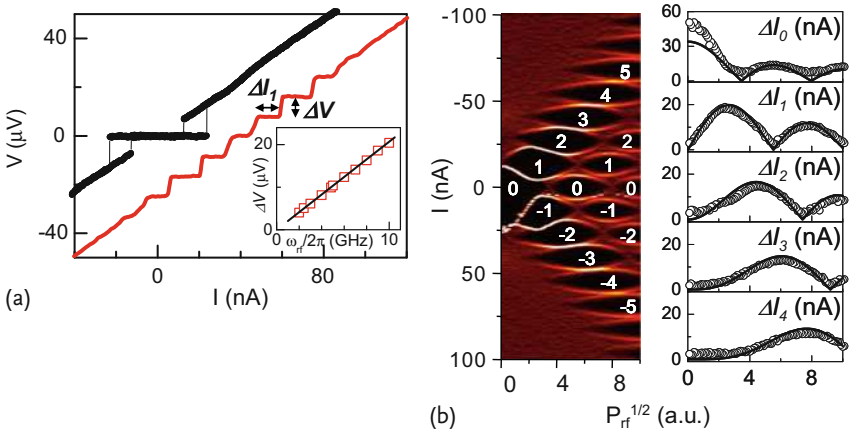

Figure 9.10 (a) $V(I)$ characteristics for device no. 3 at 40 mK, with (red) and without (black) an externally applied 4-GHz radiation (this device has $R_N = 860\,\Omega$ and $I_C = 26$ nA at $T = 40$ mK). The red trace is horizontally offset by 40 nA. The applied microwave radiation results in voltage plateaus (Shapiro steps) at integer multiples of $\Delta V = 8.3\,\mu$V. (Inset) Measured voltage spacing ΔV (symbol) as a function of microwave angular frequency ω_{RF}. The solid line (theory) shows the agreement with the AC Josephson relation $\Delta V = \hbar\omega_{RF}/(2e)$. From [30].

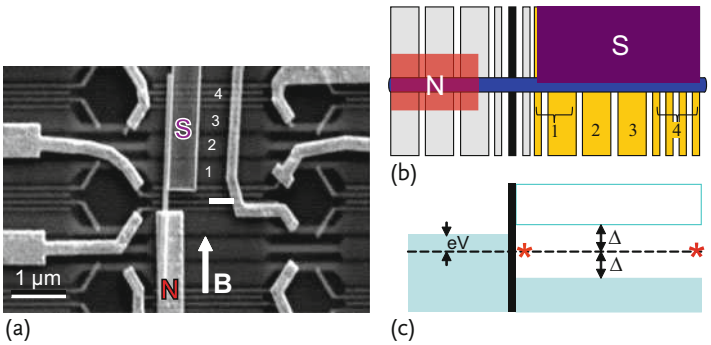

Figure 9.11 (a) Implemented version of theoretical proposals, using InSb SmNW and Nb superconductor. Scanning electron microscope image of the device with normal (N) and superconducting (S) contacts. The S contact only covers the right part of the InSb nanowire. The underlying gates, numbered 1 to 4, are covered with a dielectric. (Note that gate 1 connects two gates, and gate 4 connects four narrow gates; see (b).) (b) schematic of our device. (c) an illustration of energy states. The black rectangle indicates the tunnel barrier separating the normal part of the nanowire on the left from the wire section with induced superconducting gap, Δ. (In (a), the barrier gate is also shown in white.) An external voltage, V, applied between N and S drops across the tunnel barrier. (Red) stars, again, indicate the idealized locations of the Majorana pair. Only the left Majorana is probed in this experiment. Adapted from [24].

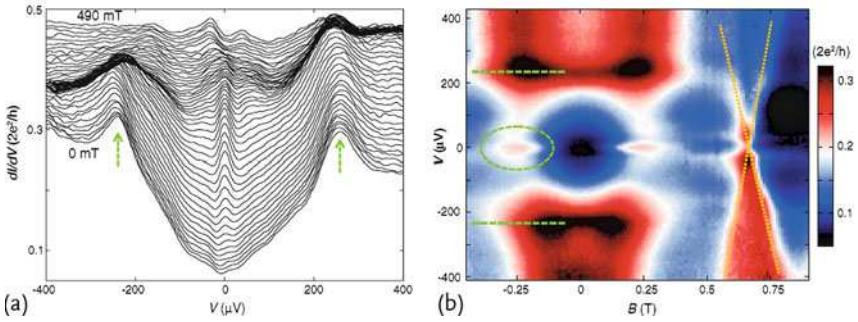

Figure 9.12 Magnetic field-dependent spectroscopy. (a) dI/dV vs. V at 70 mK taken at different B fields (from 0 to 490 mT in 10 mT steps; traces are offset for clarity, except for the lowest trace at $B = 0$). Data are from device 1. Arrows indicate the induced gap peaks. (b) Colorscale plot of dI/dV vs. V and B. The ZBP is highlighted by a dashed oval; green dashed lines indicate the gap edges. At ≈ 0.6 T, a non-Majorana state is crossing zero bias with a slope equal to ≈ 3 meV/T (indicated by sloped yellow dotted lines). Traces in (a) are extracted from (b). From [24].

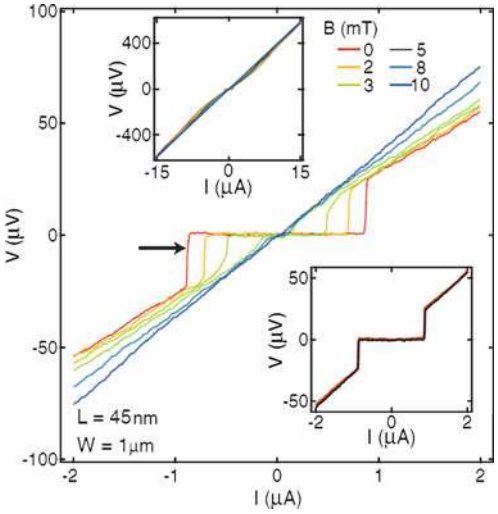

Figure 9.13 (main) V vs. I for Al-Bi_2Se_3-Al S-TI-S devices of dimensions $(L, W) = (45\text{ nm}, 1\,\mu\text{m})$ for $B = 0, 2, 3, 5, 8, 10$ mT and at a temperature of 12 mK. At $B = 0$, I_C is 850 nA, which is reduced upon increasing B. For this device, the product $I_C R_N = 30.6\,\mu$V, which is much lower than theoretically expected for conventional JJs. (Upper-left inset) I–V curves overlap for all values of B at $V \geq 2\Delta/e \sim 300\,\mu$V. (Lower-right inset) Sweeps up and down in I show little hysteresis, indicating that the junction is in the overdamped regime. Adapted from [36].